Stability of the hydrate phase assemblage in Portland composite cements containing dolomite and metakaolin after leaching, carbonation, and chloride exposure

Alisa Machner[1,3,*], Maciej Zajac[2], Mohsen Ben Haha[2], Knut O. Kjellsen[1], Mette R. Geiker[3], Klaartje De Weerdt[3]

[1]Norcem AS, R&D Department, Setreveien 2, P.O. Box 38, 3991 Brevik, Norway
[2]Heidelberg Technology Center GmbH, Oberklamweg 2-4, 69181 Leimen, Germany
[3]NTNU Department of Structural Engineering, Richard Birkelandsvei 1A, 7491 Trondheim, Norway

*Corresponding author: alisa.machner@ntnu.no
+47 45394622
ORCID-ID: 0000-0002-6334-5116

Abstract

To reduce CO_2 emissions during the production of cement and to cope with increasing demands for concrete, and thereby cement, the cement industry needs to identify new supplementary cementitious materials. These new composite cements should provide, among others, a similar or improved durability of the concrete structures. This study investigated the hydrate phase assemblage in Portland cement pastes containing dolomite or a combination of dolomite and metakaolin after leaching, carbonation, and chloride exposure. The phase assemblage and phase compositions of the exposed samples and the unexposed reference samples were investigated using TGA, XRD, and SEM-EDS. The reaction of dolomite in the cement paste resulted in the formation of hydrotalcite. It was found that, unlike most other hydration phases, hydrotalcite can withstand high degrees of leaching and carbonation. When the samples were exposed to a chloride solution, the formation of a chloride-containing hydrotalcite was observed.

Keywords:

Dolomite; Metakaolin; Blended cement; Leaching; Carbonation; Chloride exposure

1. Introduction

There is a need to identify potential new supplementary cementitious materials (SCMs) both to reduce CO_2 emissions during cement production and to cope with increasing demand for concrete and thereby cement. These new composite cements should provide, among others, a similar or improved strength development and durability compared to today's commercial cements. The use of new SCMs might change the chemistry of the cementitious system and therefore change its phase assemblage and its resistance to deterioration. Typical deterioration mechanisms for reinforced concrete include carbonation-induced or chloride-induced corrosion of the reinforcement.

During carbonation, portlandite reacts with the CO_2 dissolved in the pore solution to form $CaCO_3$. Carbonation decomposes ettringite and AFm phases and leads to the formation of $CaCO_3$, hydrous alumina and, in the case of hydrates containing sulphate, gypsum. The C-S-H phase decalcifies gradually and decomposes to amorphous silica and $CaCO_3$ [1]. The decalcification of the C-S-H phase results in an increase in the average silicate chain length and a higher Si/Ca ratio. An increased amount of calcium carbonate has been reported to form in samples with lower Si/Ca ratios and very little change in the average silicate chain length has been reported during the carbonation of the C-S-H with a high initial Si/Ca ratio [2].

When cement paste is exposed to chloride solutions, some of the chlorides will be taken up by the hydrates, while the rest will be freely available for transport in the pore solution. When Portland cement pastes are exposed to NaCl solutions, chlorides will be bound chemically in chloride-containing AFm phases like Friedel's salt or Kuzel's salt. Unlike the exposure to $CaCl_2$ solutions, exposure to NaCl solutions has been reported to result in little or no chloride being physically bound by adsorption on the C-S-H [3–7].

In addition, leaching of the cement paste, another possible deterioration mechanism, causes a drop in the pH of the pore solution and can thereby cause a change in the stability of the phase assemblage. During the leaching of a cement paste, portlandite dissolves and the C-S-H gradually decalcifies until it also decomposes together with ettringite and AFm phases, leaving only hydrous silica, alumina and iron oxide detectable in the residue [1]. However, C-S-H with a higher average silicate chain length due to the addition of SCMs containing silicon typically shows improved resistance to the leaching of calcium [8–10].

The effect on the phase assemblage of replacing 40 wt% clinker with a combination of metakaolin and dolomite or limestone has been reported in an earlier study [11]. It was shown that, depending on curing time and curing temperature, the addition of dolomite in combination with small quantities of metakaolin can lead to the formation of carbonate AFm phases and ettringite as well as a hydrotalcite-like phase (member of the hydrotalcite supergroup [12], in the following simply referred to as hydrotalcite), . The formation of hydrotalcite in Portland composite cements, especially at elevated temperatures (60 °C), has also been reported for other replacement levels of dolomite [13–15].

Hydrotalcite has shown good resistance to leaching in MgO-activated slag binder systems [16,17]. It is also reported to be a promising material for CO_2-capture technology because of its high CO_2 adsorption capacity [18]. Moreover, thermodynamic modelling of leaching has predicted that hydrotalcite will withstand harsher leaching conditions and will decompose only when the C-S-H has completely decomposed [19].

When exposed to a chloride-containing solution, hydrotalcite has been reported to show a high chloride-binding capacity due to its excellent ion exchange properties [20–22]. In cementitious systems containing slag, it has been predicted to bind more chlorides than Friedel's salt [23]. The minerals of the hydrotalcite supergroup belong to the layered double hydroxides, which are defined by the general formula $[Me^{2+}_{1-x}Me^{3+}_{x}(OH)_2]^{x+}\ [A^{m-}]_{x/m}\cdot nH_2O$. The crystal structure of hydrotalcite can be derived from that of brucite. The main layer consists of metals (here abbreviated with Me), specifically magnesium (Me^{2+}) and aluminium (Me^{3+}) hydroxide octahedra. The substitution of aluminium for magnesium in the main layer charges this layer positively. To maintain electrical neutrality, the interlayer incorporates monovalent or divalent anions (here abbreviated with A), such as OH^-, Cl^-, CO_3^{2-} or SO_4^{2-}.

Previous studies reporting on the stability of hydrotalcite or its chloride-binding capacity focused on pure synthesized hydrotalcite or on hydrotalcite formed in alkali-activated slag binder systems or slag-containing cements. These systems may deviate in pH and composition from Portland-cement-based systems, which will affect the composition and stability of the hydrotalcite formed. Moreover, the chloride-binding capacity of hydrotalcite depends strongly on the presence of carbonate ions in the pore solution [24], because divalent ions, such as carbonates, are favoured in the interlayer of hydrotalcite compared to monovalent ions, such as chlorides [20,21]. The chloride-binding capacity

of hydrotalcite could therefore be reduced for the binder systems investigated in this study, where significant amounts of dolomite are used.

In this study, we investigated the stability of the hydrate phase assemblage formed in dolomite-containing cementitious systems after leaching, carbonation, and chloride exposure with special focus on hydrotalcite. The sample preparation and curing were adapted to ensure the formation of hydrotalcite in the samples investigated [11,13]. Equivalent samples containing limestone instead of dolomite were used as references. The stability of the various hydration phases and their compositions were investigated after exposure using TGA, XRD and SEM-EDS. The results were compared to non-exposed reference samples of the same compositions and to the results of the thermodynamic modelling of one sample composition in this study.

2. Materials & Methods

2.1. Materials and cement paste preparation

For the preparation of the various binder compositions, we used a Portland cement (C) supplied by Norcem AS, to which only gypsum was added during grinding, natural dolomite (D, dolomite content: approx. 90 wt%, for more detailed information see [11]) supplied by Miljøkalk AS, natural limestone (L) supplied by Miljøkalk AS, and laboratory-grade metakaolin (M) supplied by Imerys (Metastar501). Table 1 gives the chemical composition of the materials, determined with X-ray fluorescence (XRF) and their specific surface areas determined using the Blaine method. Figure 1 shows the particle size distributions of the materials, determined using laser diffraction with a Malvern Mastersizer 2000E.

In the samples investigated, 40 wt% of the cement was replaced with dolomite (60C40D) or a combination of dolomite and metakaolin (60C35D5M). Equivalent samples containing limestone instead of dolomite (60C40L, 60C35L5M) were prepared as references. Table 2 gives an overview of the samples investigated in this study.

The pastes were prepared in batches of 540 g with a w/b ratio of 0.5 using a Braun MR 5550CA high-shear mixer (mixing procedure: mixing for 30 s, resting for 5 min, mixing for 60 s). The resulting pastes were poured into 125 mL plastic bottles, which were sealed and stored immersed up to their bottle-necks in water at 60 °C. After 3 months of curing, to ensure a high degree of reaction in the

samples, they were crushed in a jaw crusher and subsequently ground in a rotating disc mill to a particle size < 1 mm. Afterwards, 30 wt% of water was added to the ground pastes, which were then poured into tight and sealed polypropylene bottles (1 L) and stored for another 4 months at 60 °C. After a total of 7 months of curing, the samples were transferred to 20 °C for 2 weeks prior to exposure, which was also carried out at 20 °C. An overview of the sample preparation and curing is given in Table 3. The samples were cured at 60 °C, to accelerate the dolomite reaction and consequently achieve a sufficient reaction degree of dolomite within the curing time, because in a previous study the reaction of dolomite was shown to be very slow at curing temperatures of 20 °C or 38 °C [11].

2.2. Exposure conditions and reference samples

2.2.1. Leaching

50 g of each of the prepared well-hydrated ground cement pastes were poured into a cellulose extraction thimble and loaded into a Soxhlet extraction chamber in a temperature-controlled room at 20 °C. A large volume of deionized water compared to the sample size was slowly dripped onto these samples over time. When the extraction chamber was full (250 mL), it was automatically emptied again. A total of 100 L deionized water was dripped onto the sample (over approx. 6 weeks). The experimental setup was adapted from De Weerdt and Justnes [25].

2.2.2. Carbonation

Approx. 10 g of each of the prepared well-hydrated cement pastes was spread on an evaporating dish (diameter approx. 6 cm) and placed in a carbonation chamber (20 °C, 60% RH, 1% CO_2) for 34 days.

2.2.3. Exposure to chloride solutions

30 g of each of the well-hydrated cement pastes was poured into 45 mL centrifuge tubes. To these samples, 15 mL of a 2 mol/L NaCl solution was added using a volumetric pipette. The solution was prepared with laboratory-grade NaCl supplied by Merck. The samples were stored at 20 °C for at least one month to reach equilibrium. The experimental approach for the chloride exposure of the samples was the same as in [5,6].

2.2.4. Reference samples

Reference samples were prepared for all three types of exposures. The unexposed reference samples for the leached and carbonated samples were stored sealed in a temperature-controlled room at 20 °C. The reference samples for the chloride-exposed samples were prepared by adding 15 mL of deionized water to 30 g of the samples instead of a chloride solution. The XRD and TGA results of the exposed samples were compared with their reference samples, which had been stored for a similar time at 20 °C. As reference samples for the SEM-EDS analyses for all types of exposure, we used the results from an earlier study [11]. In that study, the samples were prepared with a similar cement clinker and the same SCMs, and they were cured sealed at 100% RH for 360 days at 60 °C and were prepared for SEM-EDS in a similar way.

2.3. Analyses after exposure

The samples were analysed before and after leaching, carbonation, or chloride exposure using thermogravimetric analysis (TGA), X-ray diffraction (XRD), and scanning electron microscopy (SEM). Prior to the investigation of the cement pastes, the hydration was stopped by double solvent exchange. For this, approx. 6 g of the coarsely crushed moist cement paste (whether exposed sample or reference sample) was immersed in 100 mL isopropanol, shaken for 30 seconds, and left to rest for 5 min before the isopropanol was decanted. This isopropanol treatment was performed twice, and then the sample was transferred to a filtration unit where the isopropanol was filtrated out and the paste was immersed in 20 mL petroleum ether. After 30 seconds of stirring, the suspension was left to rest for 5 minutes. The sample was then vacuum-filtrated and subsequently dried overnight in a desiccator under a slight vacuum (-0.2 bar) applied using a aspirator pump. For the TGA and XRD analyses, parts of each dried sample were crushed in a porcelain mortar until the whole sample passed through a 63 µm sieve. All samples were stored in a desiccator over silica gel and soda lime until measurement.

The TGA investigations were carried out using a Mettler Toledo TGA/DSC 3+. The 600 µL alumina crucibles were filled with approx. 150 mg of the prepared powder samples. The analysis was performed over the range of 40–900 °C with a heating rate of 10 °C/min. During the analysis, the measurement cell was purged with 50 mL/min N_2 gas. The derivate curves of the TG signal, the DTG curves, were used to detect phase changes. The DTG curves can be divided into several sections as suggested by Lothenbach et al. [26], in which the decomposition of specific phases can be detected as a weight loss. The first peak at around 100 °C is related to the ettringite (Et) decomposition and

the beginning of the dehydroxylation of the C-S-H phase. C-S-H decomposes gradually between 40 °C and 600 °C and appears as a polynomial baseline under the other peaks. Hydrotalcite (Ht) shows two weight loss events: the first at approx. 220 °C and the second at around 400 °C. The subsequent sharp peak between approx. 400 °C and 550 °C is related to the decomposition of portlandite (CH). Above 550 °C, carbonates decompose and emit CO_2.

TGA was also used to quantify the weight losses caused by the decomposition of the hydrotalcite (w_{Ht}, see Eq. 1). This was done by integrating the DTG curve in the specific temperature intervals for hydrotalcite and subtraction of a linear baseline. The resulting area represents the $w_{Ht\text{-}measured}$ in [wt%]. By applying this method the additional weight loss from the decomposition of the C-S-H phase, which appears as a baseline in this temperature region, is excluded as described in [26].

For the leaching experiments, the calculated weight losses from TGA had to be corrected for the loss of material during the leaching ($\Delta w_{leached}$ in [wt%]) as shown in Eq. 2. The $\Delta w_{leached}$ was determined by using XRF to quantify the amount of Fe_2O_3 in the well-hydrated cement pastes before ($Fe_{reference}$) and after leaching ($Fe_{leached}$), assuming that iron was not leached from the sample during exposure. When a certain percentage of the material is lost due to the leaching, the iron is relatively enriched in the leached sample compared to reference sample. From the quantifications of the iron content (see Appendix Table A.1) the loss of material during leaching was calculated to be approx. 30 wt% ±5% relative to the ignited sample weight at 900 °C. This calculation was also done for titanium oxide and led to similar results (see Appendix Table A.1).

The weight loss due to the decomposition of the hydrotalcite was normalized to the ignited weight at approx. 900 °C, which was corrected for the theoretical amount of CO_2 that is lost due to the decomposition of the carbonates (dolomite or limestone) included in the binder ($w_{900} - w_{carbonate}$). $w_{carbonate}$ was determined from the theoretical amount of dolomite or limestone in the samples ($X_{dolomite/limestone}$, which was either 40 wt% or 35 wt%), the molar mass of CO_2 ($M(CO_2)$, and the molar masses of dolomite ($M(CaMg(CO_3)_2)$ or limestone ($M(CaCO_3)$), as shown in Eq 3a) and b). In the case of the samples containing dolomite, the calculated values had to be multiplied by two prior to the normalization to the bound water content (BW) (Eq. 3a) because dolomite contains 2 mol of CO_3^{2-}. An overview of the values for $w_{Ht\text{-}measured}$, w_{900}, and BW for the various samples can be found in the Appendix (Table A.2).

$$w_{Ht} = \frac{w_{Ht-measured}}{w_{900} + w_{carbonate}} \cdot 100 \cdot (1 - \frac{\Delta w_{leached}}{100}) \quad \text{Eq. 1}$$

$$\Delta w_{leached} = 100 - \left(100 \cdot \frac{Fe_{reference}}{Fe_{leached}}\right) \quad \text{Eq. 2}$$

a) $$w_{carbonate,D} = X_{dolomite} \cdot \frac{100}{100 + BW} \cdot \frac{M(CO_2) \cdot 2}{M(CaMg(CO_3)_2)} \quad \text{Eq. 3}$$

b) $$w_{carbonate,L} = X_{limestone} \cdot \frac{100}{100 + BW} \cdot \frac{M(CO_2)}{M(CaCO_3)}$$

For the carbonation experiments, the calculated weight losses for hydrotalcite were also normalized to the sample weight at approx. 900 °C, which was assumed to be the ignited binder weight, eliminating any increased sample weight due to carbonation [27] (Eq. 1). The weight loss originating from the carbonates already present in the binder when the samples were prepared ($w_{carbonate}$) was taken into account (see Eq. 3).

The XRD analyses were carried out using a Bruker AXS D8 focus diffractometer. The diffractometer operates with CuKα radiation in a Bragg-Brentano θ–2θ geometry with a goniometer radius of 200.5 mm and is equipped with a LynxEye detector. The powder samples were front-loaded into the sample holders and queued in the sample changer until measurement. The scans ranged from 5–55 °2θ, with a step size of 0.01 °2θ and a sampling time of 0.5 s per step.

Scanning electron microscopy (SEM) was carried out using a Hitachi S-3400N microscope equipped with energy dispersive X-ray spectroscopy (EDS) from Oxford Instruments. Polished and carbon-coated sections of stopped but not ground samples were investigated. The acceleration voltage was set to 15 keV.

2.4. Thermodynamic modelling

The Gibbs free energy minimization program GEMS [28–31] was used to model changes in the hydrate phase assemblages and their volumes for sample 60C40D during leaching and carbonation exposure. The thermodynamic data from the PSI-GEMS database was supplemented with a cement-specific database (CEMDATA14 database) [32], which includes solubility products of the solids relevant for cementitious materials. For the C-S-H phase, the CSHQ model proposed by Kulik was

used [33]. The modelling of sample 60C40D was carried out for an exposure temperature of 20 °C. The composition of the Portland cement used as an input for the model was calculated from the XRF results (Table 1) by excluding TiO_2, MnO, MgO and P_2O_5 from the results and normalizing the remaining oxides to 100%. The degree of reaction of the Portland cement was assumed to be 90%, and the reaction degree of the dolomite added was assumed to be 10%. Increasing amounts of water for modelling the leaching and increasing amounts of CO_2 for modelling the carbonation were added to the hydrated binder in the model. The formation of the following phases was blocked in the modelling: CA, CA_2, hematite, magnetite, goethite, pyrite, troilite, iron, kaolinite, quartz, zeolites (chabazite), and thaumasite. This was done to prevent the formation of phases, whose formation is kinetically impossible at the conditions (temperature, pressure) of the exposure. For most of the blocked phases, 20 °C and/or the ambient pressure are too low for them to form. For thaumasite, however, this temperature is too high, because its formation has only been reported at temperatures below 20 °C [1].

3. Results

3.1. Phase changes due to sample preparation

Phase changes due to the various stages of sample preparation were monitored. An unexposed reference sample (60C35D5M) was investigated with XRD and TGA after regrinding and rehydration (α-samples), after 2 weeks at 20 °C (β-samples), and after the exposure time (γ-samples). Table 3 gives an overview of the various sample preparation stages and phase assemblage investigations.

Figure 2 shows the DTG curves of sample 60C35D5M at the various stages of sample preparation (α, β, γ). The α and β preparation stages seem only to differ in the weight loss temperature range of the carbonate decomposition. This means that the samples carbonated slightly during preparation and storage. However, a significant increase in the first weight loss interval is observed for both sample compositions between the β and γ preparation stages. Originally, the samples were stored at 60 °C, but the subsequent exposure was at 20 °C. This means that the prolonged curing of the samples at 20 °C caused the formation of additional ettringite, which was not stable at 60 °C. It is therefore important to compare the exposed samples with the γ-references, because they have been stored at 20 °C for the same time (including the exposure time). Phase changes observed between the exposed samples and the γ-reference samples should therefore be due solely to the exposure and not due to changes in phase stabilities caused by the change in curing temperature from 60 °C to 20 °C. In the following, the graphs of the various samples after leaching or carbonation are always compared with

their γ-reference samples for the TGA and XRD results. It should be noted that, for the samples exposed to 2 mol/L NaCl solution, the reference samples were exposed to deionized water for a similar time. The SEM-EDS results (BSE images, elemental maps, and point analyses) are compared with samples from an earlier study, as explained in 2.2.4.

3.2. Phase assemblage of the exposed samples

3.2.1. BSE images and elemental maps

Figure 3 shows the BSE images and elemental maps of magnesium, aluminium, calcium, silicon, oxygen, and chlorine for samples $60C40D_{reference}$, $60C40D_{leached}$, $60C40D_{CO2}$, and $60C40D_{NaCl}$. Sample $60C40D_{reference}$ is from an earlier study and was used as the reference of an unexposed sample. The BSE images and elemental maps for the mix 60C35D5M can be found in the Appendix (Figure A.1).

Figure 3a shows the BSE image and the elemental maps for the unexposed reference sample ($60C40D_{reference}$). The large uniformly grey particles, which are rich in magnesium and calcium, are partially reacted dolomite particles. The shape of the original grain boundaries of the dolomite particles before reaction is still visible due to the thin layer of C-S-H that precipitated around them at early hydration ages, and in the magnesium map. The reaction rims between the unreacted parts of the dolomite particles and their former grain boundaries are filled with hydrates, visible due to the increased oxygen counts in that area. The hydrates inside the reaction rims are rich in aluminium and magnesium, but poor in calcium and silicon, which might indicate that they are filled with hydrotalcite. This will be checked later (see 3.3.1) by SEM-EDS dot plots from measurement points taken inside these reaction rims.

Figure 3b shows that these reaction rims are still visible after leaching this sample, which indicates that hydrotalcite persisted through the leaching procedure applied. Moreover, the portlandite, which is visible due to high calcium counts in the unexposed sample, has vanished in the leached sample.

In contrast to the leached samples, the carbonated samples show relatively large uniformly bright areas within the matrix, which are rich in calcium (Figure 3c). These areas probably consist of calcium carbonate precipitated during carbonation of the calcium-containing phases in the cement paste, such as portlandite or C-S-H. The reaction rims around dolomite probably containing hydrotalcite are also visible in the carbonated samples.

In the samples exposed to a NaCl solution (Figure 3d), the chlorine map shows generally higher counts than in the other samples. Moreover, the reaction rims inside the original grain boundaries of dolomite are also rich in chlorine. This indicates that the hydrotalcite formed in these reaction rims has taken up significant amounts of chlorine.

3.2.2. TGA

Figure 4(a–c) shows the DTG curves of samples 60C40D and 60C35D5M after leaching, carbonation and chloride exposure, and their unexposed reference samples. The two binder compositions show a similar trend and are described together in the following.

The weight losses in the temperature regions of C-S-H and ettringite are significantly lower in the leached samples than in their reference samples (Figure 4a). The peak related to the decomposition of the portlandite has completely disappeared in the leached samples, but the peaks related to the decomposition of the hydrotalcite seem to be higher in the leached samples than in their references.

A significant decrease in the first weight loss interval (up to approx. 200 °C) can also be observed in the carbonated samples compared to their reference samples (Figure 4b), indicating the decomposition of ettringite and C-S-H during carbonation. The small peak in the first temperature interval of the carbonated samples might indicate the dehydration of gypsum. The decomposition of the C-S-H phase is also visible where the whole curve shifts upwards between 40–400 °C. The portlandite peak completely disappears in the carbonated samples. The two peaks related to the decomposition of hydrotalcite seem to be slightly smaller in the carbonated samples than in the reference samples.

Figure 4c shows the DTG curves of samples $60C40D_{NaCl}$ and $60C35D5M_{NaCl}$, and their reference samples which were exposed to deionized water. The first weight loss peak related to the decomposition of ettringite and the beginning dehydroxylation of C-S-H is higher in the chloride-exposed sample 60C40D than in its reference. In sample 60C35D5M, the weight loss in this temperature region seems to be unaffected by the chloride exposure. In both samples (60C40D and 60C35D5M), the two peaks related to the decomposition of hydrotalcite were changed by the exposure. The first peak (approx. 220°C) is smaller in sample 60C35D5M, and it has completely vanished in sample 60C40D. The second peak of hydrotalcite (approx. 400 °C) appears at lower temperatures. The portlandite peak is slightly smaller in samples exposed to the NaCl solution than

in their reference samples. In both exposed samples, there are several peaks in the weight loss temperature region of the carbonates, all of which can be related to the emission of CO_2 [34].

To investigate whether the amount of hydrotalcite in the samples changed during leaching or carbonation, we quantified the weight loss related to the decomposition of hydrotalcite. However, small weight losses were also observed in the hydrotalcite temperature regions for the samples containing limestone (see Appendix Figure A.2 and Figure A.3). This indicates that weight losses observed in the samples containing dolomite might not be caused solely by the decomposition of hydrotalcite formed by the reacted of dolomite. We therefore subtracted the weight losses in the samples containing limestone from those containing dolomite, so that we could quantify the hydrate weight loss in these temperature regions due solely to the reaction of dolomite.

Figure 5a shows the quantifications for the two leached samples compared to their unexposed references. The quantifications were normalized to the sample weight loss due to leaching as described in 2.2.4 (Eq. 1–2). Assuming an error of 0.1 wt%, we can see a slight increase in the weight loss of the hydrotalcite in the leached samples compared to their reference samples.

The DTG curves of the carbonated samples (Figure 4b) shifted upwards compared to those of their reference samples, because their initial mass at 40 °C increased during carbonation due to CO_2 binding, so the hydrotalcite weight loss peaks seemed lower in the carbonated samples than in the reference samples. Figure 5b shows the results of these quantifications for the carbonated samples compared to their unexposed references normalized as described in 2.2.4 (Eq. 1), to eliminate the effect of increased sample weight due to carbonation. The results of the hydrotalcite quantification for the carbonated and reference samples of 60C35D5M are very similar and within the assumed error of 0.1%. However, sample 60C40D shows a lower hydrotalcite weight loss in the carbonated sample than the reference.

3.2.3. XRD

Figure 4(d–f) shows the XRD patterns of samples 60C40D and 60C35D5M after leaching, carbonation, and chloride exposure, and their unexposed reference samples. The peak positions of ettringite (Et – 9.1 °2θ), Friedel's salt (Fs – 11.2 °2θ), Ferrite (C_4AF – 12.2 °2θ), hydrogarnet (Htg – 17.4 °2θ), hydrotalcite (Ht – approx. 11.4 °2θ), portlandite (CH – 18.1 °2θ), and brucite (Bru – 18.6 °2θ) are indicated.

Both leached samples show a higher hydrotalcite peak than their reference samples (Figure 4d). This is in good agreement with the results obtained from TGA, where a slightly increased weight loss for the hydrotalcite was measured in the leached samples than in their reference samples. Moreover, no ettringite or portlandite was detected with XRD in either of the leached samples. In sample $60C40D_{leached}$, brucite was detected, and a siliceous hydrogarnet was detected in both samples ($60C40D_{leached}$ and $60C35D5M_{leached}$). These phases seem not to be affected by leaching, because they are visible in both the leached and the reference samples.

No portlandite or ettringite peaks are observed in the carbonated samples (Figure 4e). The brucite peak observed in the reference sample 60C40D has disappeared in the carbonated sample. This might be explained by the carbonation of $Mg(OH)_2$ probably to $MgCO_3$. However, no peaks of $MgCO_3$ were observed with XRD. Generally, the XRD results agree fairly well with the results from TGA. There are no clear changes in the hydrotalcite peak between the carbonated and reference samples of 60C40D and 60C35D5M. In summary, this indicates that hydrotalcite can withstand carbonation.

The XRD patterns of the samples $60C40D_{NaCl}$ and $60C35D5M_{NaCl}$ are shown in Figure 4f alongside their reference samples, which were exposed to deionized water. It can be seen that the phase assemblage was not affected by the exposure to a 2 mol/L NaCl solution. No clear peaks of Friedel's salt can be seen in the samples exposed to NaCl.

Figure 6 shows the XRD patterns of the samples $60C40D_{NaCl}$ and $60C35D5M_{NaCl}$ and their reference samples just in the range of the first hydrotalcite peak (10–12 °2θ). The peak positions of Friedel's salt, hydrotalcite and chloride-containing hydrotalcite (Ht_{Cl} – approx. 11.1–11.3 °2θ) are indicated together with the exact angle of their reflections. The peaks of the hydrotalcite in samples exposed to NaCl have shifted to lower angles compared to those of the hydrotalcite in the reference samples exposed to deionized water.

3.3. Phase composition

3.3.1. Composition of the hydrotalcite

Figure 7 shows the results of the point analyses of the reaction rims around the unreacted dolomite grains in samples 60C40D and 60C35D5M after a) leaching, b) carbonation, and c) chloride exposure. The results of these analyses are plotted as the Mg/Si ratio over the Al/Si ratio.

Most of the points for sample 60C35D5M, and some of the points for sample 60C40D plot along linear lines, which are indicated by dotted lines. This suggests the presence of a reaction product with a fixed Mg/Al ratio, which does not contain significant amounts of silicon. It can, therefore, be identified as hydrotalcite [35,36]. The Mg/Al ratios of the hydrotalcite for the exposed samples and their references are shown by the slope of the dotted lines and are summarized in Table 4.

The Mg/Al ratio is higher for sample 60C40D than for sample 60C35D5M, regardless of the exposure. This difference can be explained by the 5 wt% of metakaolin in sample 60C35D5M, which acts as a source for aluminium and therefore lowers the Mg/Al ratio of the hydrotalcite. This effect has been described for similar binder compositions [11] and for cements containing ground granulated blast furnace slag either in various amounts or with various aluminium contents [37,38].

For the mix 60C40D, there is a bigger spread in the EDS-points of the leached or chloride-exposed samples than in the carbonated sample. In leached or chloride-exposed samples, some of the points spread towards a higher magnesium content. This is due to intermixing with brucite, which is shown by a peak in XRD, both in the reference and in the leached and chloride-exposed 60C40D samples. Intermixing with brucite was not observed for sample $60C40D_{CO2}$, probably because brucite was not stable after carbonation.

Figure 8 shows the results of the point analyses for the samples $60C40D_{NaCl}$ and $60C35D5M_{NaCl}$ and the unexposed reference sample plotted as the Cl/Ca ratio over the Al/Ca ratio. The plots confirm the findings from TGA and XRD that the hydrotalcite in the samples exposed to NaCl contains chlorides, whereas the results from the unexposed reference sample show no chloride uptake in the hydrotalcite.

3.3.2. Composition of the C-S-H phase

We also investigated the composition of the C-S-H in the exposed samples. All graphs show the results from an earlier study [11] as unexposed reference samples with a similar binder composition.

In Figure 9, the results of the point analyses for the leached samples are plotted as the Al/Ca ratio over the Si/Ca ratio. In this graph, the composition of the C-S-H can be determined as shown by the dashed ovals [1]. The C-S-H phase in mature Portland cement pastes usually has a Si/Ca ratio of

approx. 0.5, as shown by the reference samples. This value is significantly lower than the Si/Ca ratio determined in the leached samples in this study, which have a Si/Ca ratio in the range of approx. 1.5–2.0. Moreover, the leached samples showed a less defined C-S-H composition than the reference samples. This is probably due to the decalcification of the C-S-H phase, which causes a significant spread in the results when they are normalized to calcium. It should also be mentioned that the setup applied in this study did not leach the samples homogenously. This inhomogeneity might also cause a spread in the results, as shown previously where the same setup was used [25].

Figure 10 shows the C-S-H composition as the Mg/Si ratio over the Al/Si ratio for the samples $60C40D_{leached}$ and $60C35D5M_{leached}$ compared to their reference samples with similar compositions. This graph shows the Al/Si ratio of the C-S-H as the intersection between the X-axis and the lines described by the data points. The leached samples show similar results to the reference samples, which indicates that the Al/Si ratio of the C-S-H was not affected by the leaching and that the aluminium uptake in the C-S-H was similar in both samples. The slope of the lines in Figure 10 represents the Mg/Al ratio of the matrix. The Mg/Al ratios of the C-S-H are very similar to those of the hydrotalcite listed in Table 4, which indicates that hydrotalcite can also be found finely intermixed with the C-S-H in the matrix.

The C-S-H compositions in the carbonated samples were also measured with SEM-EDS, as shown in Figure 11. Unlike the results for the leached samples, the results of these point analyses do not show a clear composition of the C-S-H phase. Instead, the results spread in two directions: towards lower and higher Si/Ca ratios.

Figure 12 shows the Mg/Si ratio over the Al/Si ratio of the C-S-H of the carbonated samples 60C40D and 60C35D5M compared to the non-carbonated reference samples. Before carbonation, sample 60C35D5M showed a higher Al/Si ratio of the C-S-H due to the metakaolin added in this sample. In contrast to the results from the leached samples (Figure 10), the Al/Si ratio decreased in the carbonated sample 60C35D5M to approximately the same value as for sample 60C40D. Similarly to the leached samples, the Mg/Al ratios of the matrix show very similar results compared to the Mg/Al ratios of the hydrotalcite listed in Table 4, which indicates that hydrotalcite is finely intermixed with the C-S-H in the matrix.

Figure 13 shows the Al/Ca ratio over the Si/Ca ratio of the samples 60C40D$_{NaCl}$ and 60C35D5M$_{NaCl}$ alongside the results of the unexposed reference samples. The C-S-H in sample 60C35D5M shows a higher Si/Ca ratio than sample 60C40D.

Figure 14 shows the Cl/Al ratio over the Si/Ca ratio for these samples and illustrates the chloride uptake of the C-S-H. The results of the unexposed reference samples plot almost completely on the X-axis, indicating little or no chloride content in these samples, whereas the samples exposed to NaCl show a higher chloride content. This confirms the observations made with the elemental maps in 3.2.1, where sample 60C40D$_{NaCl}$ showed generally higher counts of chlorine also in the matrix. This also agrees well with the observations made from Figure 10 and Figure 12, which indicated that hydrotalcite is also finely intermixed with the C-S-H in the matrix.

3.4. Thermodynamic modelling of the phase assemblage during leaching and carbonation

Figure 15 shows the phase assemblage modelled for sample 60C40D in contact with an increasing amount of water. First, the portlandite, and then the ettringite, monocarbonate and C-S-H all decompose. The calcite predicted by the thermodynamic modelling originated from the reaction of dolomite, which we assumed to have a reaction degree of 10%. Ferrihydrite ($Fe_2O_3 \cdot 0.5H_2O$) is predicted due to the decomposition of AFm and AFt phases, which were modelled to contain a certain amount of iron due to the high degree of reaction we assumed for the Portland cement (90%), but it was not observed experimentally. Hydrotalcite seemed to be stable until approx. 28000 L of deionized water had been added. Hydrous silica and aluminium have also been reported in the residue of an extremely leached cement sample [1], but were not predicted by the thermodynamic model. This difference can probably be explained by the modelling, which represents an idealized case leading to the full dissolution of these phases.

Figure 16 shows the phase assemblage modelled for sample 60C40D with increasing amounts of CO_2 added (in grams). First, the portlandite, and then the C-S-H, ettringite and monocarbonate all decompose, and an increasing amount of calcite is formed. As with the leaching model, ferrihydrite is predicted due to the decomposition of the iron-containing AFm and AFt phases. Strätlingite forms as an intermediate state between C-S-H and amorphous silica. The stable phases predicted at high levels of added CO_2 are calcite, ferrihydrite, gypsum, magnesite, natrolite, and gibbsite, but some of these were not observed experimentally. This can be explained either by the small quantities of some

of these phases, which make their identification difficult, or by the fact that our system had not reached equilibrium.

4. Discussion

4.1. Comparison of the results of the thermodynamic modelling with the phase assemblage experimentally observed

In the following, we compare the thermodynamic modelling of the leaching (Figure 15) and carbonation (Figure 16) of sample 60C40D with the phase assemblages experimentally observed (Figure 4). The dashed rectangles drawn in Figure 15 and Figure 16 indicate the areas of the experimentally observed phase assemblages in the thermodynamic modelling. Within the rectangles, all the portlandite has decomposed, and C-S-H and ettringite have started to decompose, while the hydrotalcite is still stable.

The thermodynamic modelling predicted the decomposition of portlandite with increasing amounts of water or CO_2 added to the system. This is in agreement with the phase assemblage experimentally observed in this study, because portlandite was not observed with TGA or XRD after carbonation or leaching. The decomposition of portlandite is caused, in the case of leaching, by its dissolution in the leachate, and, in the case of carbonation, by its reaction with the CO_2 dissolved in the pore solution to form $CaCO_3$ [1].

During carbonation, ettringite is reported to decompose, while hydrous alumina, calcite, and gypsum form instead [1]. This is only partially in agreement with our results. No ettringite peak was observed in the carbonated samples with XRD, but no peak of gypsum was detected either with XRD, and only a small peak of gypsum was observed with TGA. The reason why gypsum was not detected with XRD might be that the gypsum (11.6°2θ) and hydrotalcite (11.4°2θ) peak positions overlapped slightly, or that too little gypsum was formed. During leaching, the thermodynamic model also predicts the dissolution of ettringite. This was confirmed by the experimental results, where no peak of ettringite was observed with XRD and the weight loss of ettringite in TGA was significantly lower in the samples after leaching.

The general shift upwards of the DTG curves after carbonation or leaching indicates the reduced amount of C-S-H, as predicted by the thermodynamic modelling. The thermodynamic modelling

predicted the decomposition of the C-S-H starting when the portlandite has decomposed during the carbonation or leaching of the samples, which is also according to the literature [1].

Hydrotalcite was observed experimentally with XRD and TGA and predicted by the thermodynamic modelling before and after leaching. This confirms the findings of Feng et al. [19]. Hydrotalcite was also observed experimentally in the samples after carbonation. It should be noted that in the thermodynamic model magnesite ($MgCO_3$) is predicted for high amounts of added CO_2, but hydrotalcite has been reported to be able to take up significant amounts of CO_2 and therefore to withstand a high degree of carbonation [18]. The reason for different results in the thermodynamic modelling might be that the hydrotalcite used for the modelling is a hydroxide-hydrotalcite that is not stable at high partial pressures of CO_2, or it might be due to kinetic effects of the transformation of hydrotalcite to $MgCO_3$.

It should be noted that the dashed rectangles in Figure 15 indicate a greater amount of water in the modelling compared to the experimental 100 L. This can be explained by the use of a Soxhlet extractor in our experimental setup. The samples were immersed in a small amount of deionized water for a short time, and then the Soxhlet extractor emptied itself automatically and was slowly filled again. This meant that the samples were not able to reach equilibrium with the total amount of water added. In the modelling, however, increasing amounts of water were added, which were in equilibrium with the solids present. The presence of monocarbonate in the modelling, which was not observed experimentally, can be explained by the sample preparation. The thermodynamic modelling was performed at 20 °C, while the samples were cured at 60 °C for approx. 7 months prior to the exposure at 20 °C. This indicates that due to this high-temperature curing the monocarbonate was not stable in our experimental samples. This is in accordance with the findings from Lothenbach et al., who reported a decreasing amount of monocarbonate in samples cured at such high temperatures [39].

Taking into account the limitations described above, the thermodynamic modelling agreed fairly well with the phase assemblage experimentally observed with XRD and TGA. The thermodynamic model confirms that the hydrotalcite formed by the reaction of dolomite in a cementitious system is a stable hydration product, which can withstand leaching, or carbonation within the range tested.

4.2. Composition of the C-S-H

Because the exposure to a 2 mol/L chloride solution did not change the phase assemblage or the Si/Ca ratio of the C-S-H, these samples can be used to elucidate the effect of metakaolin addition on the composition of the C-S-H. We measured a higher Si/Ca ratio of the C-S-H in samples containing 5 wt% metakaolin than in sample 60C40D. This can be explained by the pozzolanic reaction of metakaolin in sample 60C35D5M, which increases the Si/Ca ratio and the silicate chain length of the C-S-H [40,41]. This has also been reported previously for other silicon-containing SCMs, e.g. silica fume [9,42,43].

Sample 60C35D5M$_{NaCl}$ shows a higher Si/Ca ratio of the C-S-H than the unexposed reference sample from an earlier study [11]. This can be explained by the sample preparation in this study, which resulted in a higher degree of reaction of the cement and metakaolin. The reference samples from an earlier study were cured in sealed tubes for 360 days and probably show a less mature C-S-H phase than the C-S-H in this study.

The increased Si/Ca ratio in the C-S-H in the leached samples indicates a severe decalcification of the C-S-H phase due to the leaching. This effect of leaching on the Si/Ca ratio of the C-S-H is in agreement with previous findings [1,44].

The SEM-EDS point analyses of the C-S-H after carbonation show a spread in the results towards higher and lower Si/Ca ratios (Figure 11). This indicates the presence of calcium carbonate and a silicon-rich phase. A similar observation is reported by Leemann et al. [45]. It can be explained by the gradual decalcification of the C-S-H until it finally decomposes to amorphous silica and $CaCO_3$ [1]. In contrast, Belda Revert et al., who used a similar cement, observed only a decrease in the Si/Ca ratio of the C-S-H due to the fine intermixing of decalcified C-S-H and calcium carbonate [27]. In this study, however, the calcium carbonate precipitated in large lumps, rather than finely intermixed with the C-S-H. The lumps of calcium carbonate can be seen, for example, in a larger picture of the carbonated sample 60C35D5M (see Appendix Figure A.4), where the calcium carbonate (Cc) is indicated with arrows. The large lumps are probably due to the sample preparation in our study. We crushed the samples after 3 months of curing to a grain size <1 mm and added 30 wt% of additional water. These actions were taken in order to maximize the hydration degree of the samples, but they also significantly coarsened the microstructure. This method of sample preparation also changed the transport of CO_2 and H_2O in the samples during exposure.

Moreover, we observed a decrease in the aluminium uptake of the C-S-H for carbonated samples compared to the reference samples, which is in agreement with the results of Belda Revert et al., who observed a decrease in the Al/Ca ratio for C-S-H in carbonated mortar samples containing 30 wt% fly-ash after carbonation [27].

4.3. Quantification of the amount of hydrotalcite in the samples after leaching and carbonation

The fact that sample 60C40D shows a higher weight loss in the temperature region of hydrotalcite in the reference than in the carbonated sample (Figure 5b) might be due to the presence of brucite in the reference sample, which can also result in a weight loss in the temperature region of hydrotalcite. In the carbonated samples, brucite ($Mg(OH)_2$) was not observed with XRD because it probably had reacted to $MgCO_3$ and therefore did not contribute to the weight losses in this temperature region. Brucite and calcite have been reported to be the reaction products of the dedolomitization reaction of dolomite and portlandite [46–48], as shown in Eq. 4.

$$CaMg(CO_3)_2 + Ca(OH)_2 \rightarrow Mg(OH)_2 + 2CaCO_3 \quad \text{Eq. 4}$$

However, in cementitious systems, where other ions are present (e.g. Al), hydrotalcite has been reported to form [11,13–15], as shown in Eq. 5.

$$6CaMg(CO_3)_2 + 2Al(OH)_3 + 6Ca(OH)_2 + 3H_2O \rightarrow Mg_6Al_2(OH)_{18}\cdot 3(H_2O) + 12CaCO_3 \quad \text{Eq. 5}$$

In an earlier study focusing on a similar binder composition, no clear peaks of brucite could be detected [11]. The formation of brucite solely in sample 60C40D in this study might be explained by the sample preparation including the crushing and rehydrating of the samples, which considerably increased the reaction degree of the system and probably also the reaction degree of the dolomite. This would increase the magnesium available in the system. There was no metakaolin in sample 60C40D, so the amount of aluminium in the system is relatively low, which together with the high magnesium content in the sample led to the formation of brucite. No brucite was detected in sample 60C35D5M, because sufficient aluminium was available in this sample containing 5 wt% metakaolin.

In the leached samples, the amount of hydrotalcite quantified with TGA was slightly higher than in the unleached reference samples (Figure 5 a). This could have been an artefact of the low sample weight of the leached samples compared to their references, but the quantifications with TGA were normalized by the XRF results, which would eliminate this effect. Another possible explanation could be the increased dissolution rate of dolomite in solutions at a lower pH [49–52]. Leaching with 100 L of deionized water lowered the pH of the samples to approx. 10.7 according to the modelling results. However, this drop in pH due to leaching is probably not big enough to increase the dissolution rate of dolomite, because significant changes is the dolomite dissolution rate were reported only for pH values < 9 [52].

4.4. Composition of the hydrotalcite

Mg/Al ratios of approx. 2 are commonly reported for hydrotalcite-like phases in cementitious systems [13,35,38,53–56]. However, higher Mg/Al ratios are also possible because the natural mineral hydrotalcite has a Mg/Al ratio of 3 [57]. The high Mg/Al ratios in our study (60C40D:3.2, 60C35D5M: 2.4) might be explained by the relatively pure dolomite (dolomite content approx. 90 wt%) and small metakaolin additions used in our study.

The values of the Mg/Al ratios of the hydrotalcite after the various exposures were similar to the Mg/Al ratios of hydrotalcite formed in unexposed samples of an earlier study [11]. This indicates that the hydrotalcite formed was not only stable during leaching, carbonation, and chloride exposure, but also did not change its composition with regard to its Mg/Al ratio.

The phase assemblage seemed to be only slightly affected by the exposure to a 2 mol/L NaCl solution and was therefore not discussed in detail above. For the hydrotalcite, however, a shift in the peak position was observed with XRD when the samples were exposed to NaCl. This shift to lower angles has been reported previously and can be related to the formation of a chloride-containing hydrotalcite (Ht_{Cl}) [24]. A possible intermixing with Friedel's salt cannot be excluded, because the peaks of the chloride-containing hydrotalcite are slightly asymmetric, which could indicate the presence of small amounts of Friedel's salt. The TGA signal of the hydrotalcite also changed during chloride exposure. These changes in the TGA signal have previously been reported for pure synthesized hydrotalcite [24], but the temperatures of these peaks in the present study differ from those reported by Ke et al. [24], probably because the hydrotalcite in this study was formed in a

674 cementitious system rather than as a pure phase. The chloride-uptake of the hydrotalcite was
675 confirmed qualitatively by the SEM-EDS investigations (Figure 8).

676

677 ## 4.5. Outlook

678 This study represents a first step in investigating composite cements containing dolomite and
679 metakaolin with regard to durability. The stability in various environments of hydrotalcite, one of
680 the main reaction products of dolomite in Portland cement-based pastes, indicates that its formation
681 can potentially be beneficial for the durability of the resulting concrete. A next step for evaluating the
682 durability would be to conduct suitable performance tests on concrete with this new composite
683 cement compared with today's commercial cements.

684

685

5. Conclusions

This study presents a screening of the stability of the hydrate phase assemblage after selected exposures. Well-hydrated cement paste samples in which 40 wt% of the cement was replaced by dolomite or by a combination of dolomite and metakaolin were investigated after carbonation, leaching, and chloride exposure. The exposed samples were compared to unexposed reference samples. From the results obtained, the following conclusions can be drawn:

- Leaching caused severe decalcification of the C-S-H and decomposition of the portlandite and ettringite. The Mg/Al ratio of the hydrotalcite did not change during leaching.
- Carbonation resulted in an almost complete decomposition of the C-S-H phase and ettringite, and the consumption of the portlandite. Hydrotalcite seemed to resist carbonation without changes in its Mg/Al ratio.
- The exposure to a 2 mol/L NaCl solution resulted in the formation of a chloride-containing hydrotalcite. The Mg/Al ratio of the hydrotalcite did not change during exposure to NaCl.

It can be concluded that the hydrotalcite formed in the reaction of dolomite in a Portland composite cement is a stable hydration product in the environments tested.

6. Acknowledgements

The authors would like to thank the industrial PhD programme of the Norwegian Research Council (Project: 241637) and the Heidelberg Technology Center for their financial support. Alisa Machner would also like to thank Tone Østnor from SINTEF and the student assistants Petter Hemstad and Kristine Nøttveit from NTNU for their help with the various exposures and analyses.

7. References

[1] H.F.W. Taylor, Cement Chemistry, 2nd ed., Telford, London, 1997.

[2] T.F. Sevelsted, J. Skibsted, Carbonation of C–S–H and C–A–S–H samples studied by ^{13}C, ^{27}Al and ^{29}Si MAS NMR spectroscopy, Cem Concr Res 71 (2015) 56–65.

[3] Z. Shi, M.R. Geiker, K. De Weerdt, T.A. Østnor, B. Lothenbach, F. Winnefeld, J. Skibsted, Role of calcium on chloride binding in hydrated Portland cement–metakaolin–limestone blends, Cem Concr Res 95 (2017) 205–216.

[4] O. Wowra, M.J. Setzer, Sorption of chlorides on hydrated cement and C_3S pastes, in: M.J. Setzer, R. Auberg (Eds.), Frost Resistance of Concrete, E & FN Spon, London, 1997, pp. 147–153.

[5] K. De Weerdt, A. Colombo, L. Coppola, H. Justnes, M.R. Geiker, Impact of the associated cation on chloride binding of Portland cement paste, Cem Concr Res 68 (2015) 196–202.

[6] K. De Weerdt, D. Orsáková, M.R. Geiker, The impact of sulphate and magnesium on chloride binding in Portland cement paste, Cem Concr Res 65 (2014) 30–40.

[7] A. Delagrave, J. Marchand, J.-P. Ollivier, S. Julien, K. Hazrati, Chloride Binding Capacity of Various Hydrated Cement Paste Systems, Advanced Cement Based Materials 6 (1997) 28–35.

[8] Matte V., Moranville M., Durability of Reactive Powder Composites: influence of silica fume on the leaching properties of very low water/binder pastes, Cement and Concrete Composites 21 (1999) 1–9.

[9] J.J. Gaitero, I. Campillo, A. Guerrero, Reduction of the calcium leaching rate of cement paste by addition of silica nanoparticles, Cem Concr Res 38 (2008) 1112–1118.

[10] J. Jain, N. Neithalath, Analysis of calcium leaching behavior of plain and modified cement pastes in pure water, Cement and Concrete Composites 31 (2009) 176–185.

[11] A. Machner, M. Zajac, M. Ben Haha, K.O. Kjellsen, M.R. Geiker, K. De Weerdt, Limitations of the hydrotalcite formation in Portland composite cement pastes containing dolomite and metakaolin, Manuscript submitted for publication (2017).

[12] S.J. Mills, A.G. Christy, J.-M.R. Génin, T. Kameda, F. Colombo, Nomenclature of the hydrotalcite supergroup: Natural layered double hydroxides, Mineral. Mag. 76 (2012) 1289–1336.

[13] M. Zajac, S.K. Bremseth, M. Whitehead, M. Ben Haha, Effect of $CaMg(CO_3)_2$ on hydrate assemblages and mechanical properties of hydrated cement pastes at 40 °C and 60 °C, Cem Concr Res 65 (2014) 21–29.

[14] M. Zajac, M. Ben Haha, Hydration of limestone and dolomite cement, in: Proceedings of the 14th International Congress on the Chemistry of Cement, 2015.

[15] M. Zajac, W. Dienemann, G. Bolte, Comparative experimental and virtual investigations of the influence of calcium and magnesium carbonates on reacting cement, in: Proceedings of the 13th International Congress on the Chemistry of Cement, Madrid, 2011.
[16] F. Jin, A. Al-Tabbaa, Evaluation of novel reactive MgO activated slag binder for the immobilisation of lead and zinc, Chemosphere 117 (2014) 285–294.
[17] F. Jin, F. Wang, A. Al-Tabbaa, Three-year performance of in-situ solidified/stabilised soil using novel MgO-bearing binders, Chemosphere 144 (2016) 681–688.
[18] Q. Wang, Z. Wu, H.H. Tay, L. Chen, Y. Liu, J. Chang, Z. Zhong, J. Luo, A. Borgna, High temperature adsorption of CO_2 on Mg–Al hydrotalcite: Effect of the charge compensating anions and the synthesis pH, Catalysis Today 164 (2011) 198–203.
[19] P. Feng, C. Miao, J.W. Bullard, A model of phase stability, microstructure and properties during leaching of portland cement binders, Cement and Concrete Composites 49 (2014) 9–19.
[20] S. Miyata, Anion-Exchange Properties of Hydrotalcite-Like Compounds, Clays and Clay Minerals 31 (1983) 305–311.
[21] L. Châtelet, J.Y. Bottero, J. Yvon, A. Bouchelaghem, Competition between monovalent and divalent anions for calcined and uncalcined hydrotalcite: anion exchange and adsorption sites, Colloids and Surfaces A 111 (1996) 167–175.
[22] O. Kayali, M.S.H. Khan, M. Sharfuddin Ahmed, The role of hydrotalcite in chloride binding and corrosion protection in concretes with ground granulated blast furnace slag, Cement and Concrete Composites 34 (2012) 936–945.
[23] H. Ye, X. Jin, W. Chen, C. Fu, N. Jin, Prediction of chloride binding isotherms for blended cements, Computers and Concrete 17 (2016) 655–672.
[24] X. Ke, S.A. Bernal, J.L. Provis, Uptake of chloride and carbonate by Mg-Al and Ca-Al layered double hydroxides in simulated pore solutions of alkali-activated slag cement, Cem Concr Res 100 (2017) 1–13.
[25] K. De Weerdt, H. Justnes, The effect of sea water on the phase assemblage of hydrated cement paste, Cement and Concrete Composites 55 (2015) 215–222.
[26] B. Lothenbach, P. Durdzinski, K. De Weerdt, Thermogravimetric Analysis, in: K.L. Scrivener, R. Snellings, B. Lothenbach (Eds.), A Practical Guide to Microstructural Analysis of Cementitious Materials, CRC Press Taylor & Francis Group, Boca Raton, 2015, pp. 177–211.
[27] A. Belda Revert, K. De Weerdt, K. Hornbostel, M.R. Geiker, Investigation of the effect of partial replacement of Portland cement by fly ash on carbonation using TGA and SEM-EDS, in: O.M. Jensen, K. Kovler, N. de Belie (Eds.), International RILEM Conference on Materials, Systems and

776 Structures in Civil Engineering: Conference segment on Concrete with Supplementary
777 Cementitious Materials, Rilem Publications S.A.R.L., 2016, pp. 413–422.
778 [28] D. Kulik, GEM-Selektor v.3.3, available at: http://gems.web.psi.ch/.
779 [29] B. Lothenbach, F. Winnefeld, Thermodynamic modelling of the hydration of Portland cement,
780 Cem Concr Res 36 (2006) 209–226.
781 [30] T. Wagner, D.A. Kulik, F.F. Hingerl, S.V. Dmytrieva, GEM-Selektor geochemical modeling
782 package: TSolMod library and data interface for multicomponent phase models, The Canadian
783 Mineralogist 50 (2012) 1173–1195.
784 [31] D.A. Kulik, T. Wagner, S.V. Dmytrieva, G. Kosakowski, F.F. Hingerl, K.V. Chudnenko, U.R. Berner,
785 GEM-Selektor geochemical modeling package: Revised algorithm and GEMS3K numerical
786 kernel for coupled simulation codes, Comput Geosci 17 (2013) 1–24.
787 [32] Thermodynamic database, provided by EMPA, available at:
788 https://www.empa.ch/web/s308/thermodynamic-data.
789 [33] D.A. Kulik, Improving the structural consistency of C-S-H solid solution thermodynamic
790 models, Cem Concr Res 41 (2011) 477–495.
791 [34] A. Machner, M. Zajac, M. Ben Haha, K.O. Kjellsen, M.R. Geiker, K. De Weerdt, Chloride-binding
792 capacity of hydrotalcite in cement pastes containing dolomite and metakaolin, Manuscript
793 submitted for publication.
794 [35] M. Ben Haha, B. Lothenbach, G. Le Saout, F. Winnefeld, Influence of slag chemistry on the
795 hydration of alkali-activated blast-furnace slag – Part I: Effect of MgO, Cem Concr Res 41
796 (2011) 955–963.
797 [36] A.M. Harrisson, N.B. Winter, H.F.W. Taylor, Microstructure and Microchemistry of Slag Cement
798 Pastes, Mater. Res. Soc. Symp. Proc. 85 (1986) 213–222.
799 [37] R. Taylor, I.G. Richardson, R.M.D. Brydson, Composition and microstructure of 20-year-old
800 ordinary Portland cement–ground granulated blast-furnace slag blends containing 0 to 100%
801 slag, Cem Concr Res 40 (2010) 971–983.
802 [38] M. Ben Haha, B. Lothenbach, G. Le Saout, F. Winnefeld, Influence of slag chemistry on the
803 hydration of alkali-activated blast-furnace slag – Part II: Effect of Al_2O_3, Cem Concr Res 42
804 (2012) 74–83.
805 [39] B. Lothenbach, F. Winnefeld, C. Alder, E. Wieland, P. Lunk, Effect of temperature on the pore
806 solution, microstructure and hydration products of Portland cement pastes, Cem Concr Res 37
807 (2007) 483–491.

[40] C.A. Love, I.G. Richardson, A.R. Brough, Composition and structure of C–S–H in white Portland cement–20% metakaolin pastes hydrated at 25 °C, Cem Concr Res 37 (2007) 109–117.
[41] W. Kunther, Z. Dai, J. Skibsted, Thermodynamic modeling of hydrated white Portland cement–metakaolin–limestone blends utilizing hydration kinetics from ^{29}Si MAS NMR spectroscopy, Cem Concr Res 86 (2016) 29–41.
[42] H. Justnes, Kinetics of Reaction in Cementitious Pastes Containing Silica Fume as Studied by ^{29}Si MAS NMR, in: P. Colombet, H. Zanni, A.R. Grimmer, P. Sozzani (Eds.), Nuclear Magnetic Resonance Spectroscopy of Cement-Based Materials, Springer Berlin Heidelberg, Berlin, Heidelberg, 1998, pp. 245–268.
[43] J.E. Rossen, B. Lothenbach, K.L. Scrivener, Composition of C–S–H in pastes with increasing levels of silica fume addition, Cem Concr Res 75 (2015) 14–22.
[44] A. Dauzères, G. Achiedo, D. Nied, E. Bernand, S. Alahrache, B. Lothenbach, Magnesium perturbation in low-pH concretes placed in clayey environment – solid characterizations and modeling, Cem Concr Res 79 (2016) 137–150.
[45] A. Leemann, P. Nygaard, J. Kaufmann, R. Loser, Relation between carbonation resistance, mix design and exposure of mortar and concrete, Cement and Concrete Composites 62 (2015) 33–43.
[46] E. Garcia, P. Alfonso, M. Labrador, S. Galí, Dedolomitization in different alkaline media: Application to Portland cement paste., Cem Concr Res 33 (2003) 1443–1448.
[47] S. Galí, C. Ayora, P. Alfonso, E. Tauler, M. Labrador, Kinetics of dolomite-portlandite reaction: Application to Portland cement concrete, Cem Concr Res 31 (2001) 933–939.
[48] X. Zhang, F.P. Glasser, K.L. Scrivener, Reaction kinetics of dolomite and portlandite, Cem Concr Res 66 (2014) 11–18.
[49] F. Mittermayr, A. Baldermann, C. Baldermann, G.H. Grathoff, D. Klammer, S.J. Köhler, A. Leis, L.N. Warr, M. Dietzel, Environmental controls and reaction pathways of coupled de-dolomitization and thaumasite formation, Cem Concr Res 95 (2017) 282–293.
[50] L. Chou, R.M. Garrels, R. Wollast, Comparative study of the kinetics and mechanisms of dissolution of carbonate minerals, Chemical Geology 78 (1989) 269–282.
[51] O.S. Pokrovsky, S.V. Golubev, J. Schott, A. Castillo, Calcite, dolomite and magnesite dissolution kinetics in aqueous solutions at acid to circumneutral pH, 25 to 150 °C and 1 to 55 atm pCO_2: New constraints on CO_2 sequestration in sedimentary basins, Chemical Geology 265 (2009) 20–32.

[52] J.W. Morse, R.S. Arvidson, The dissolution kinetics of major sedimentary carbonate minerals, Earth-Science Reviews 58 (2002) 51–84.
[53] G. Fornasari, R. Glöckler, M. Livi, A. Vaccari, Role of the Mg/Al atomic ratio in hydrotalcite-based catalysts for NOx storage/reduction, Applied Clay Science 29 (2005) 258–266.
[54] S.-D. Wang, Alkali-activated slag: hydration process and development of microstructure, Advances in Cement Research 12 (2000) 163–172.
[55] S.-D. Wang, K.L. Scrivener, Hydration products of alkali activated slag cement, Cem Concr Res 25 (1995) 561–571.
[56] S. Adu-Amankwah, L. Black, M. Zajac, The effect of sulphates on limestone containing composite cements, in: University of Aberdeen (Ed.), 35th Cement and Concrete Science Conference, 2015.
[57] R. Allmann, H.P. Jespen, Die Struktur des Hydrotalkits, Neues Jahrbuch für Mineralogie (Monatshefte) 12 (1969) 544–551.

8. Tables

Table 1: Chemical composition of the Portland cement, dolomite, limestone and metakaolin used, determined with XRF [wt%] and their Blaine specific surface areas [m^2/kg].

Oxide	**C** **Portland cement**	**D** **Dolomite**	**L** **Limestone**	**M** **Metakaolin**
SiO_2	19.91	0.52	0.12	52.18
Al_2O_3	5.15	0.01	0.06	44.92
TiO_2	0.282	0.00	0.00	1.14
MnO	0.062	0.00	0.00	0.00
Fe_2O_3	3.42	0.04	0.03	0.62
CaO	62.73	31.52	55.12	0.12
MgO	2.34	20.14	0.41	0.04
K_2O	1.09	0.00	0.01	0.18
Na_2O	0.48	0.00	0.00	0.17
SO_3	3.16	0.00	0.02	0.14
P_2O_5	0.109	0.01	0.00	0.07
LOI	1.07	46.79	43.57	0.29
Sum (1050°C)	**99.80**	**99.03**	**99.34**	**99.87**
Blaine [m^2/kg]	**416**	**340**	**370**	**987**

Table 2: Overview of the various binder compositions investigated [wt%]. The sulphate content of the cement was set to 3.2 wt%.

Name	**C** **Portland cement**	**D** **Dolomite**	**L** **Limestone**	**M** **Metakaolin**
60C40D	60	40	-	-
60C35D5M	60	35	-	5
60C40L	60	-	40	-
60C35L5M	60	-	35	5

Table 3: Overview of the various sample preparation stages and phase assemblage investigations with XRD and TGA.

Sample preparation stage	**XRD & TGA investigation**
Paste mixing 1st curing at 60°C for 3 months Grinding & re-hydration	
	α
2nd curing at 60°C for 4 months Transferring samples (20°C, 2 weeks)	
	β
Start of exposure (at 20 °C)	
End of exposure	**γ**

867 Table 4: Mg/Al ratios of the hydrotalcite formed in the samples 60C40D and 60C35D5M after leaching, carbonation, or
868 chloride exposure. As reference, the Mg/Al ratios of the hydrotalcite in samples from an earlier study are given [11].

	Mg/Al	
Exposure	**60C40D**	**60C35D5M**
Reference	3.2	2.4
Leaching	3.0	2.6
Carbonation	3.1	2.4
NaCl	3.2	2.4

869

870

871

9. Figures

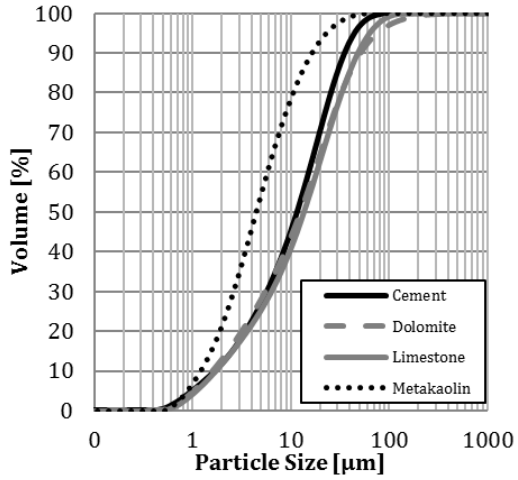

Figure 1: Particle size distributions of the materials used, determined using laser diffraction.

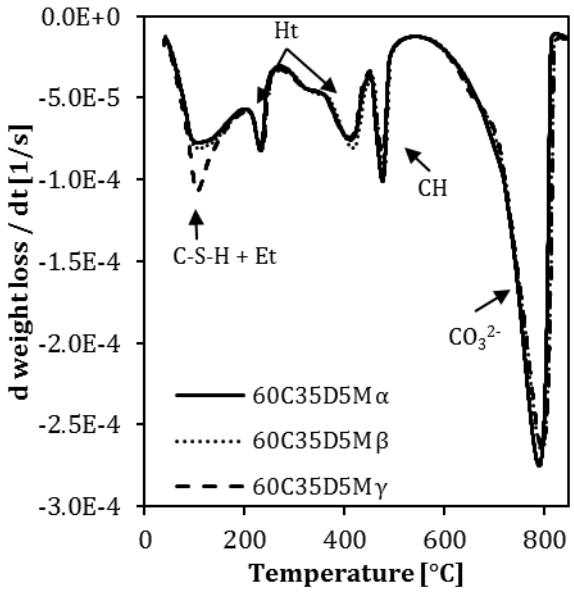

Figure 2: DTG curves of the various stages of sample preparation (α, β, γ, see Table 3) of the reference samples 60C35D5M.

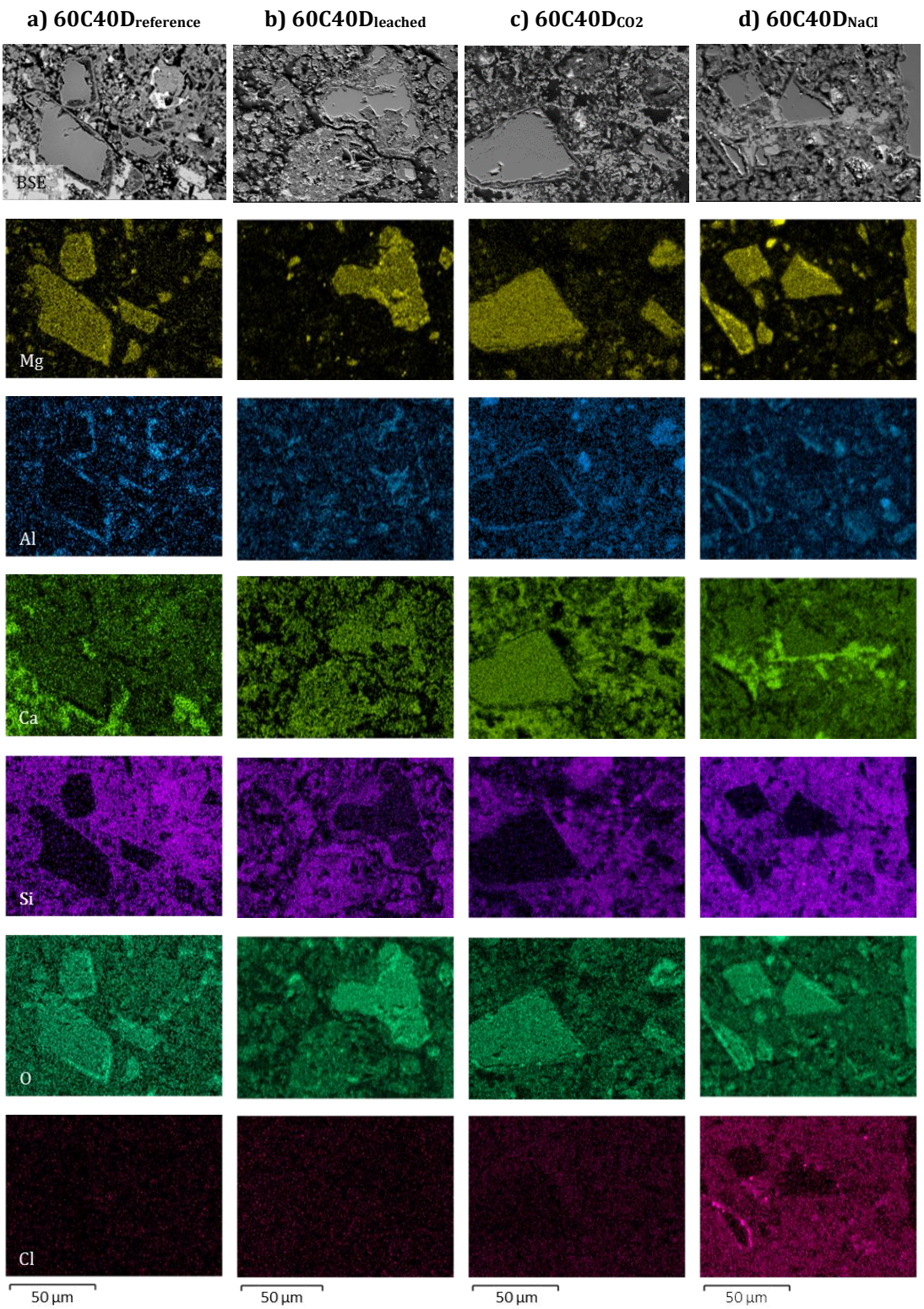

Figure 3: BSE image and elemental maps of magnesium, aluminium, calcium, silicon, oxygen, and chlorine for the samples 60C40D$_{reference}$, 60C40D$_{leached}$, 60C40D$_{CO2}$, and 60C40D$_{NaCl}$. The unexposed reference sample is from an earlier study [11].

878

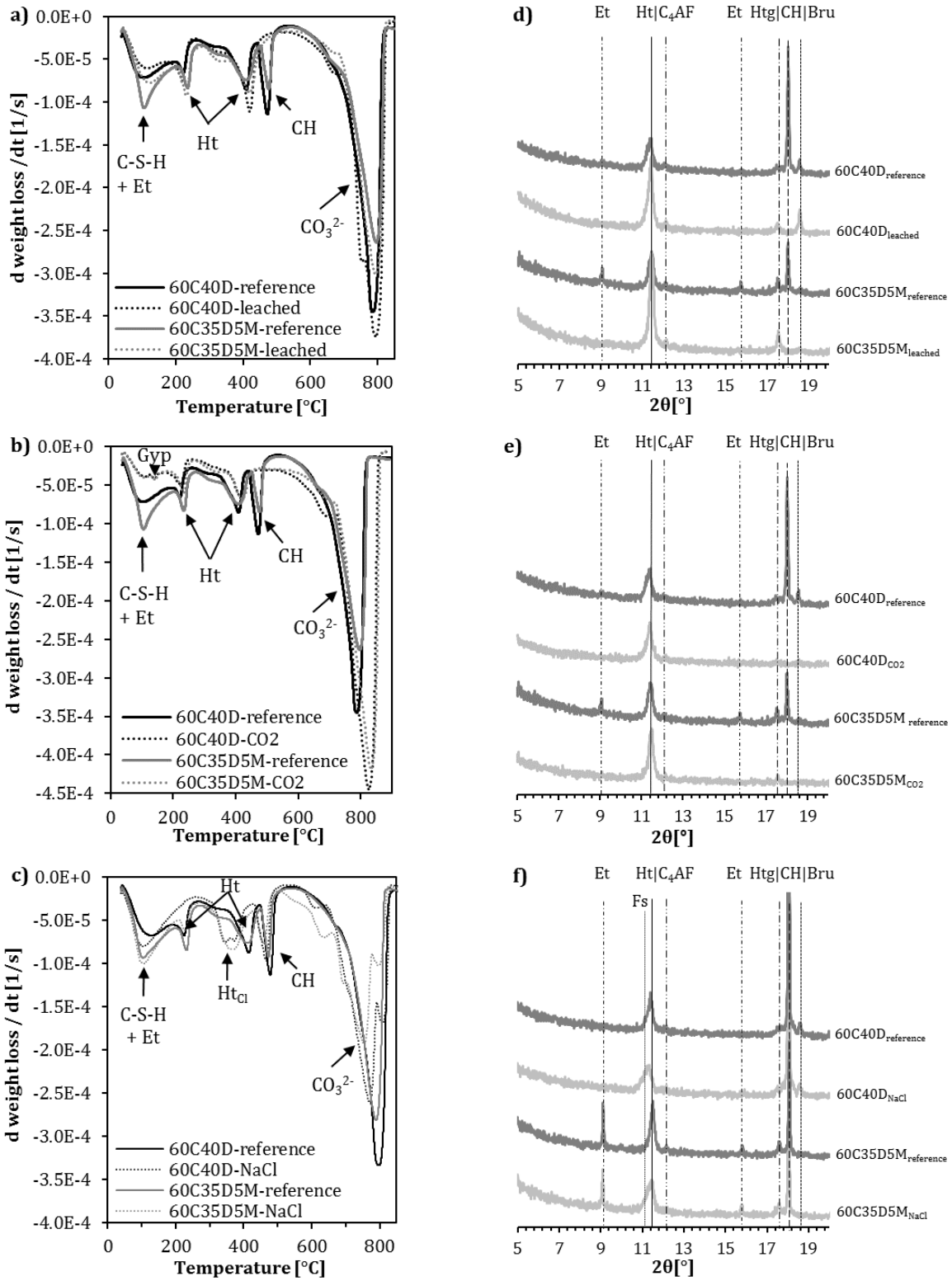

Figure 4: Phase assemblage of the samples 60C40D and 60C35D5M after leaching, carbonation, or chloride exposure determined with TGA (from 40–900 °C) and XRD (shown from 5–19.5 °2θ). The results of unexposed reference samples are also shown. The following abbreviations are used: ettringite (Et), hydrotalcite (Ht), chloride-containing hydrotalcite (Ht_{Cl}), portlandite (CH), carboantes (CO_3^{2-}), Friedel's salt (Fs), ferrite (C_4AF), siliceous hydrogarnet (Htg), brucite (Bru).

879

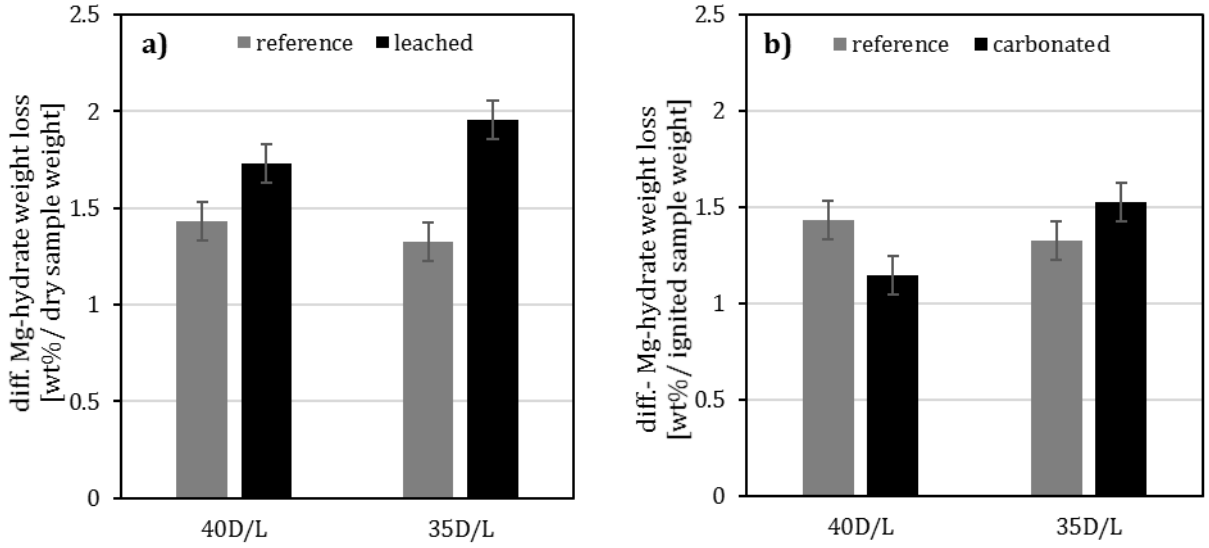

Figure 5: Difference in the weight loss in the hydrotalcite temperature region between samples containing dolomite and limestone in the unexposed reference samples and the exposed samples after a) leaching and b) carbonation.

880

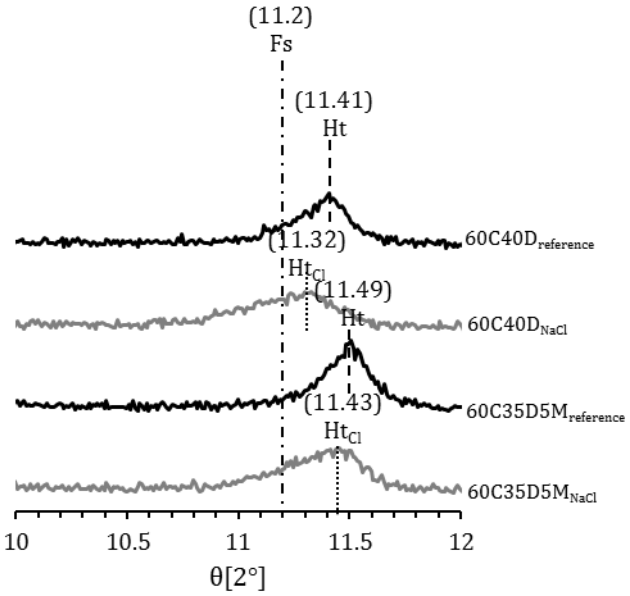

Figure 6: XRD patterns (zoomed in to 10-12 °2θ) of the samples $60C40D_{NaCl}$, $60C35D5M_{NaCl}$, and their reference samples exposed to deionized water.

881

882

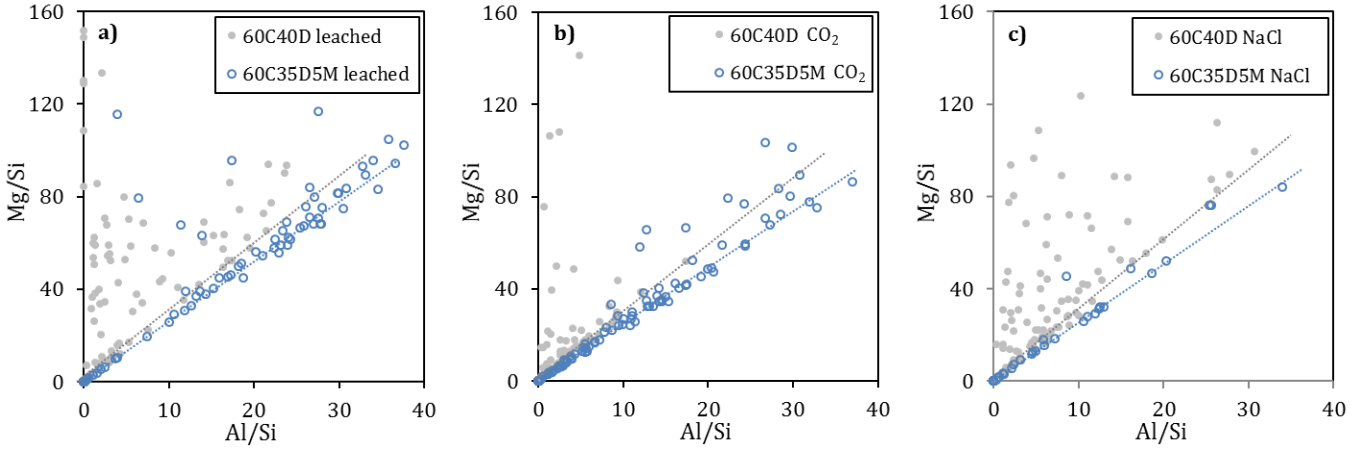

Figure 7: Mg/Si ratio over the Al/Si ratio for the point analyses of the reaction rims around the dolomite grains of samples 60C40D and 60C35D5M after a) leaching, b) carbonation, and c) chloride exposure.

883

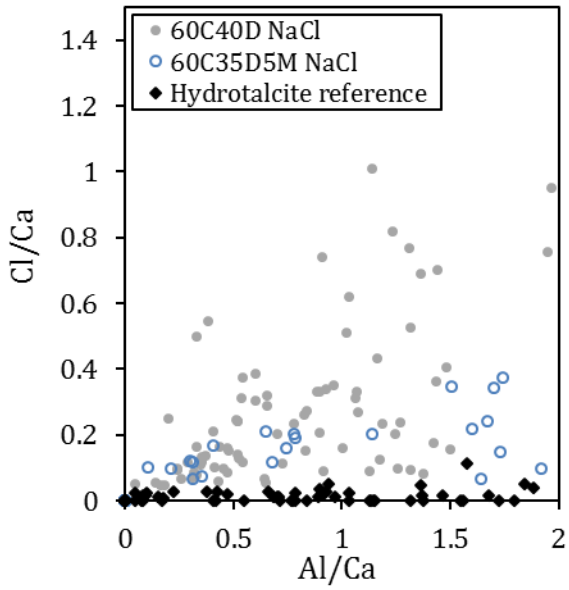

Figure 8: Cl/Ca ratio over the Al/Ca ratio for the point analyses of the reaction rims around the dolomite grains of samples $60C40D_{NaCl}$ and $60C35D5M_{NaCl}$ and the unexposed reference sample [11].

884

885

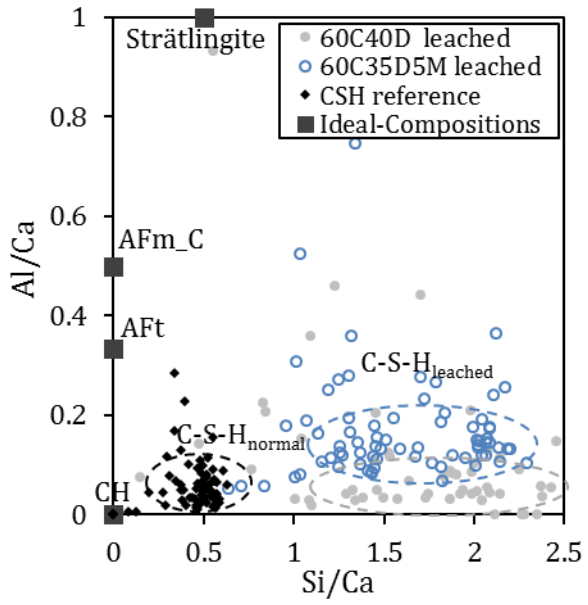

Figure 9: Al/Ca ratio over the Si/Ca ratio for the point analyses of the matrix of the leached samples 60C40D and 60C35D5M. The results of the C-S-H point analyses from an earlier study are shown as a reference for samples that have not been leached [11].

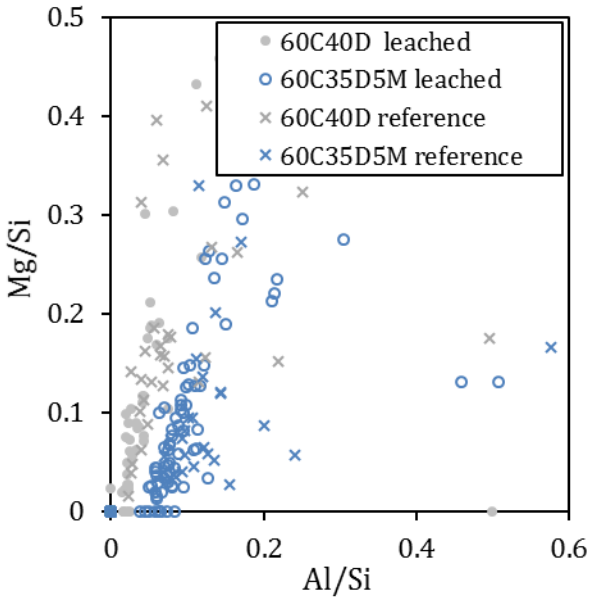

Figure 10: Mg/Si ratio over the Al/Si ratio for the point analyses of the matrix of the leached samples 60C40D and 60C35D5M. The results of the C-S-H point analyses from an earlier study are shown as a reference for samples that have not been leached [11].

886

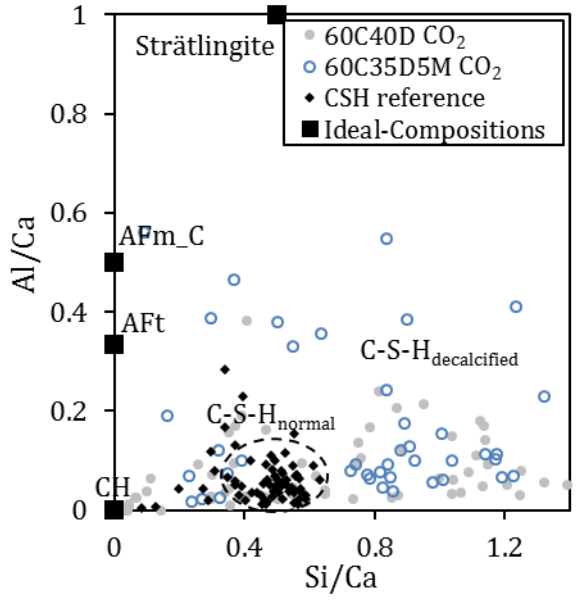

Figure 11: Al/Ca ratio over the Si/Ca ratio for the point analyses of the matrix of the carbonated samples 60C40D and 60C35D5M. The results of the C-S-H point analyses from an earlier study are shown as a reference for samples that have not been carbonated [11].

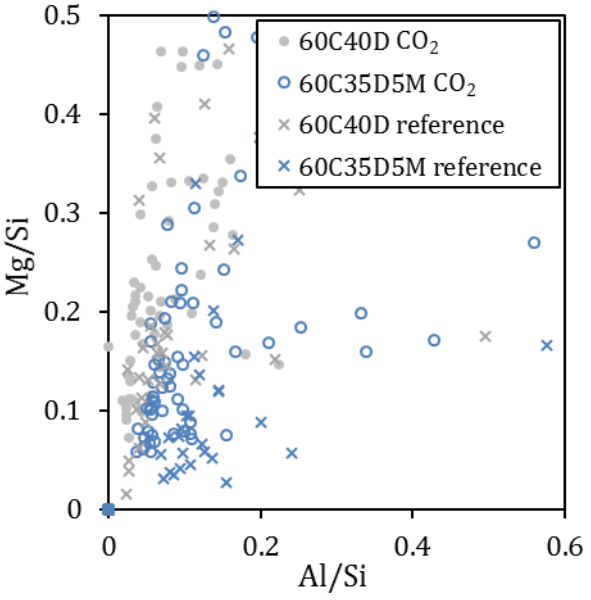

Figure 12: Mg/Si ratio over the Al/Si ratio for the point analyses of the matrix of the carbonated samples 60C40D and 60C35D5M. The results of the C-S-H point analyses from an earlier study are shown as a reference for samples that have not been carbonated [11].

887

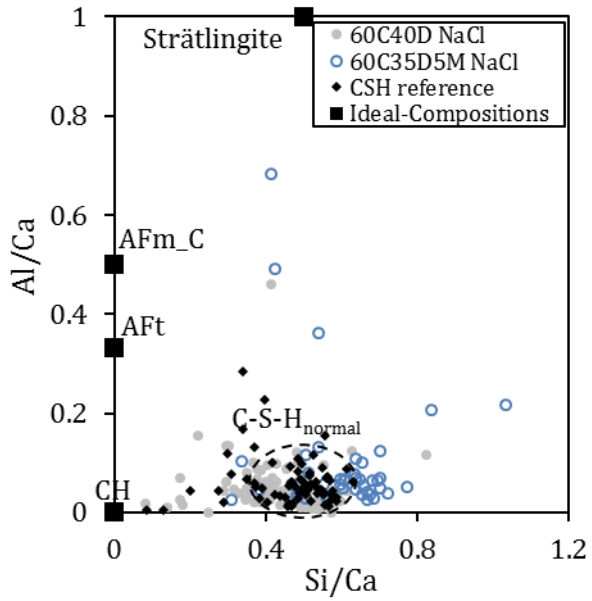

Figure 13: Al/Ca ratio over the Si/Ca ratio for the point analyses of the matrix of the samples 60C40D and 60C35D5M exposed to NaCl. The results of the C-S-H point analyses from an earlier study are shown as a reference for unexposed samples [11]

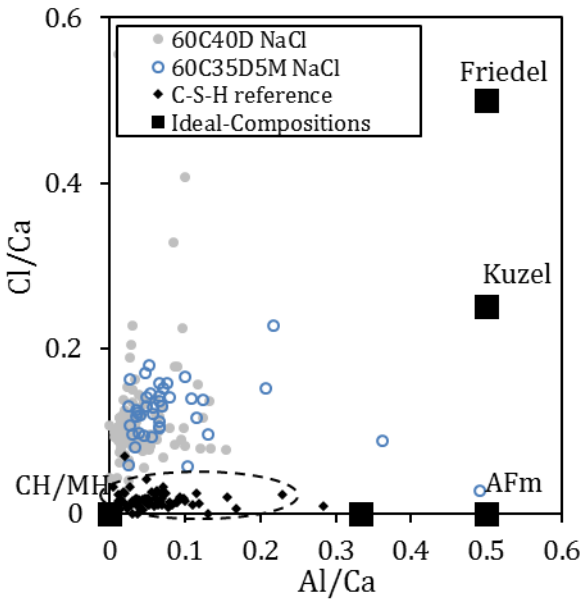

Figure 14: Cl/Ca ratio over the Al/Ca ratio for the point analyses of the matrix of the samples 60C40D and 60C35D5M exposed to NaCl. The results of the C-S-H point analyses from an earlier study are shown as a reference for unexposed samples [11]

888

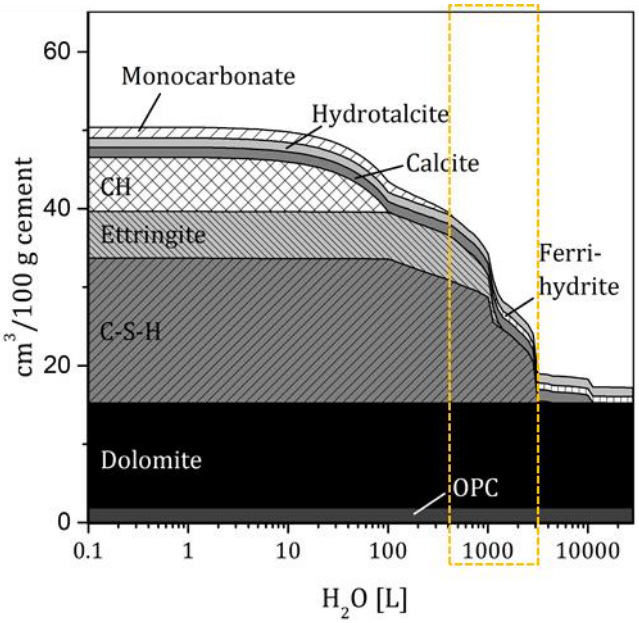

Figure 15: Results of the thermodynamic modelling of the effect of leaching on the phase assemblage in sample 60C40D. The dashed rectangle indicates the phase assemblage experimentally observed with TGA and XRD.

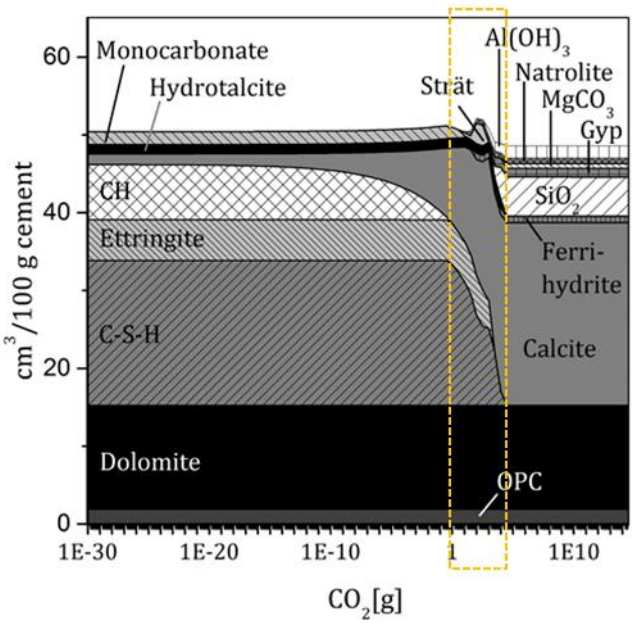

Figure 16: Results of the thermodynamic modelling of the effect of carbonation on the phase assemblage in sample 60C40D. The dashed rectangle indicates the phase assemblage experimentally observed with TGA and XRD

889

890

891

10. Appendix

Table A.1: Ti and Fe contents [wt%] on the ignited weight basis of the various samples determined with XRF and the weight losses of the samples after leaching ($\Delta w_{leached}$) calculated with Eq. 2 [wt%].

		60C40D	60C35D5M	60C40L	60C35L5M	Average
Ti	$Ti_{reference}$	0.14	0.19	0.14	0.19	
	$Ti_{leached}$	0.19	0.29	0.22	0.26	
	$Ti_{reference}/Ti_{leached}$	0.74	0.65	0.66	0.72	
	$\Delta w_{leached}$	**26**	**35**	**34**	**28**	**30±4**
Fe	$Fe_{reference}$	1.70	1.77	1.71	1.74	
	$Fe_{leached}$	2.27	2.83	2.38	2.45	
	$Fe_{reference}/Fe_{leached}$	0.75	0.63	0.72	0.71	
	$\Delta w_{leached}$	**25**	**37**	**28**	**29**	**30±5**

Table A.2: Overview of the $w_{Ht\text{-}measured}$, w_{900}, and BW values of the various samples used for the calculations in Eq. 1 and Eq.3.

Sample	Exposure	$w_{Ht\text{-}measured}$ [wt%]	w_{900} [wt%]	BW [wt%]
60C40D	reference	1.5	67.3	14.2
	leached	2.5	67.8	12.8
	CO_2	1.0	61.6	9.1
60C35D5M	reference	1.4	68.3	15.8
	leached	2.7	65.6	13.7
	CO_2	1.3	63.4	9.7
60C40L	reference	0.3	68.3	13.7
	leached	0.3	66.9	10.2
	CO_2	0.1	62.1	6.2
60C35L5M	reference	0.3	69.7	13.9
	leached	0.4	69.2	11.4
	CO_2	0.1	64.0	7.1

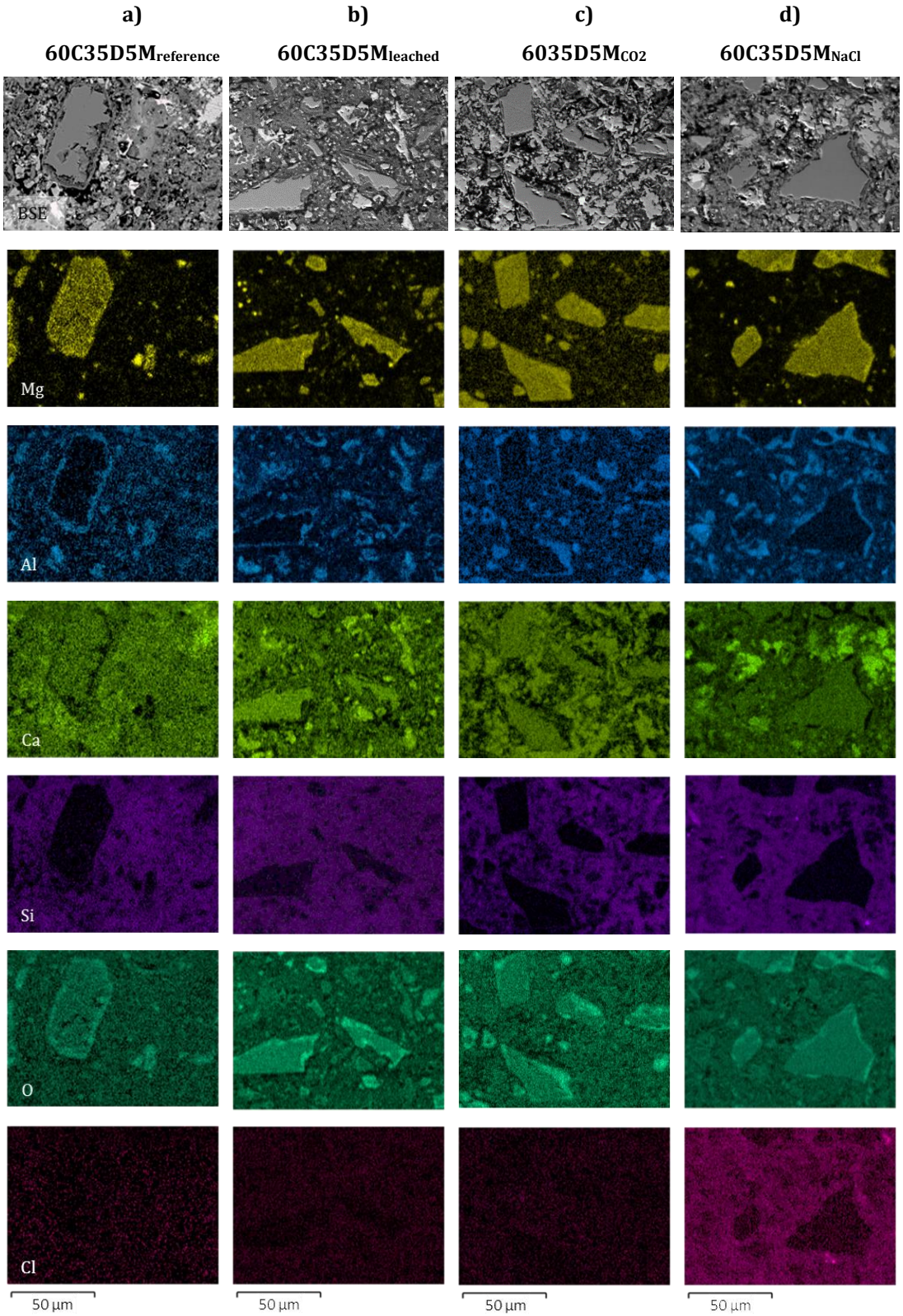

Figure A.1: BSE image and elemental maps of magnesium, aluminium, calcium, silicon, oxygen, and chlorine for the samples 60C35D5M$_{reference}$, 60C35D5M$_{leached}$, 60C35D5M$_{CO2}$, and 60C35D5M$_{NaCl}$. The unexposed reference sample is from an earlier study [11].

900

901

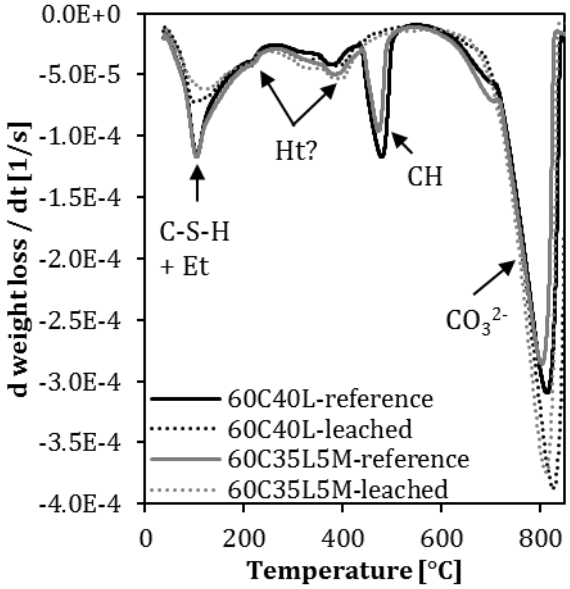

Figure A.2: DTG curves of the samples 60C40L and 60C35L5M after leaching and their unexposed reference samples.

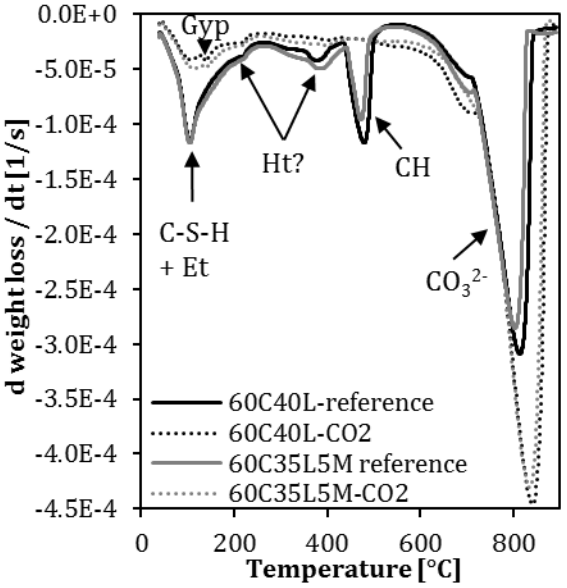

Figure A.3: DTG curves of the samples 60C40L and 60C35L5M after carbonation and their unexposed reference samples.

902

903

904

6035D5M$_{CO2}$

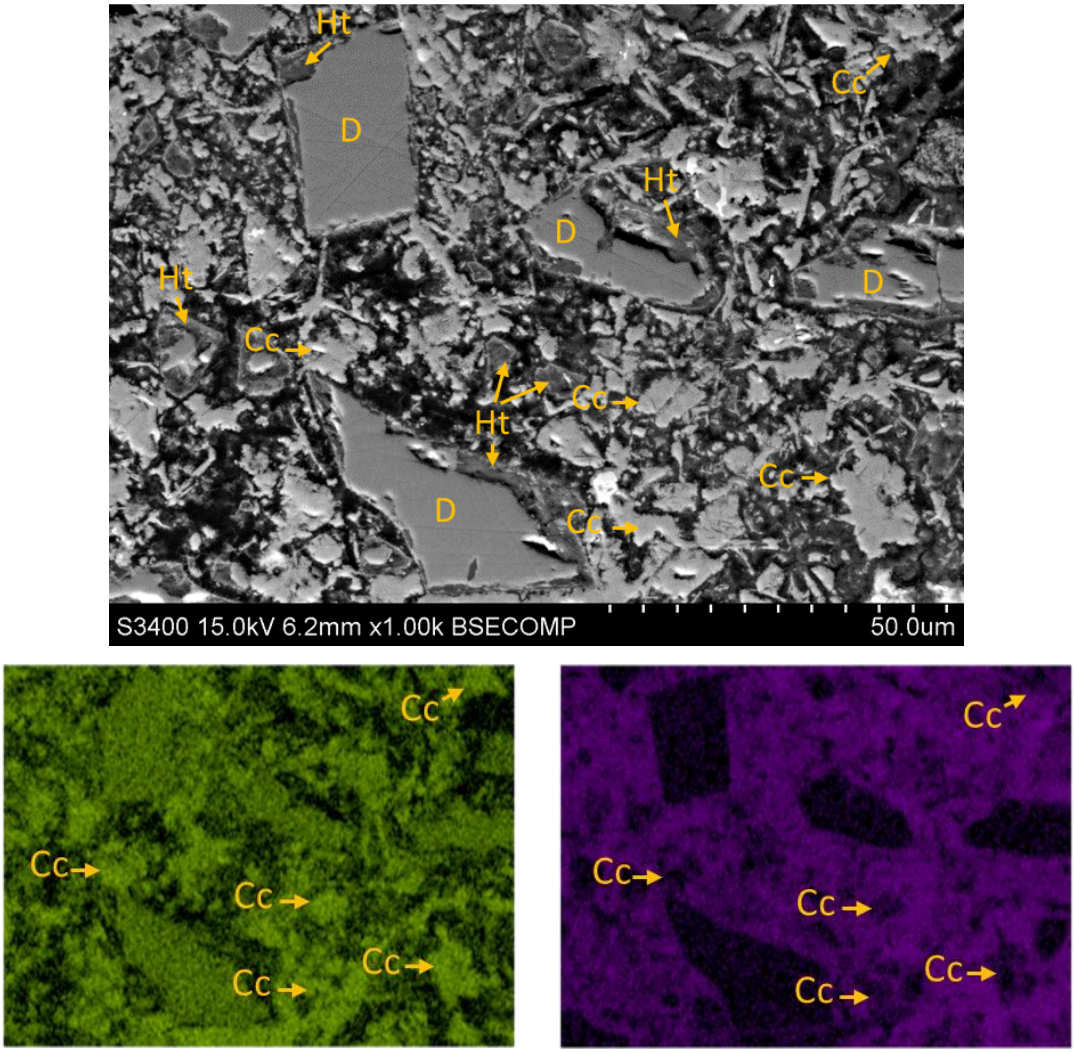

Figure A.4: BSE image and elemental maps of calcium and silicon for sample 60C35D5M CO_2. Areas of dolomite (D), calcite (Cc) and hydrotalcite (Ht) are indicated.

905